A fibre-reinforced poroviscoelastic finite element model for the Achilles tendon

Anna Gustafsson

2014

Master's Thesis

Faculty of Engineering, LTH

Department of Biomedical Engineering

Supervisors: Hanifeh Khayyeri and Hanna Isaksson

Abstract

Tendons connect muscles to bone and consist of a complex structure of almost parallel collagen fibres embedded in a hydrated matrix. The mechanical behaviour of tendons is viscoelastic and highly non-linear. The Achilles tendon is the largest tendon in the body and it is essential for walking and jumping. It is the most frequently ruptured tendon in humans and today there is no consensus on what is the best treatment. To be able to improve and develop suitable treatments for tendon injuries more knowledge in tendon mechanics is necessary.

Computational models can increase the understanding of tendon mechanics and also be used to predict tendon rupture or the mechanical response in unknown loading situations. There are different models used for tendons today but most of them provide a mathematical description of the mechanical behaviour without any direct coupling to the physiological structure of tendons.

In this study, a structural fibre-reinforced poroviscoelastic finite element model is developed for the Achilles tendon, based on a model for articular cartilage. It is assumed that the collagen fibres, the non-fibrillar matrix and the fluid flow contribute to the total stress in the tendon and specific constitutive models are used for the different components. The fibres are modelled as non-linear viscoelastic one dimensional units, the surrounding matrix is modelled as a neo-Hookean material and the permeability is assumed to be strain-dependent.

The model is curve fitted to experimental test data from rat Achilles tendons subjected to cyclic loading by optimizing nine material parameters. In total, the model is curve fitted to 21 specimens from two different data sets and two average tendons representing each set.

It was found that an exponential stress-strain relationship for the collagen fibres was necessary to capture the non-linear behaviour of the Achilles tendon. With this exponential formulation, very good curve fits were obtained for all specimens from both groups and for the average tendons. Statistical analyses show that the optimized material parameters from the two data sets are not significantly different.

The proposed model can accurately simulate the Achilles tendons under cyclic loading and it identifies the collagen fibres to be the most important load bearing structural parts in tensile loading. This model also looks promising for predicting the general mechanical behaviour of the Achilles tendon under other similar loading conditions.

Preface

This master's thesis has been carried out at the Department of Biomedical Engineering at Lund University in collaboration with the Department of Clinical and Experimental Medicine, Orthopaedics at Linköping University, during spring 2014.

I would like to thank my supervisors Hanifeh Khayyeri and Hanna Isaksson for introducing me to the interesting field of biomechanics and for giving me valuable guidance and support throughout this project. I would also like thank everyone in the biomechanics group, I really enjoyed my coffee breaks with you!

Anna Gustafsson
Lund, June 2014

Contents

1 Introduction

Tendons connect muscles to bone and transmit forces from muscle contractions, producing joint movement. Tendons also improve joint stability and act as shock absorbers and energy storage sites (Nordin and Frankel, 2012). The tendon is a complex structure of collagen fibres embedded in a hydrated matrix, built to withstand high repetitive loads and large deformations. It is a highly non-linear viscoelastic material that can be compared to a fibre-reinforced composite.

There are different families of tendons, grouped according to their functionality. Here, the focus will be on the Achilles tendon, which is subjected to high tensile loads. The Achilles tendon connects the calf muscle *gastrocnemius*, to the heel bone *calcaneus*, see figure 1, and it is essential for walking and jumping. It is the most frequently ruptured tendon in humans and today there is no consensus on what is the best treatment (Holm et al., 2014). Improved knowledge in tendon mechanics is necessary so that treatments and rehabilitation protocols can be properly designed.

Figure 1: The Achilles tendon.
Picture taken from http://www.arthroscopy.com/sp09009.htm

Computational modelling can help us to better understand the mechanics of tendons and also predict the mechanical response at different loading situations. A mechanical model for healthy tissue can be developed to predict failure and later on also be the starting point for modelling tendon healing.

An appropriate tendon model requires large strain theory and must be able to capture the viscoelastic properties at different loads. Many tendon models are phenomenological, providing a mathematical description of the mechanical behaviour without any direct coupling to the physiological structure.

1.1   Aim

The aim of this thesis is to develop a material model for the Achilles tendon based on an existing model for articular cartilage. The tendon model proposed here is a structural model considering collagen fibres, solid matrix and fluid flow as contributors to the total stress. This model tries to address the importance of each of the different structural parts. The model will be validated against experimental data from Eliasson et al. (2007).

2   Background

2.1   Tendons

Tendon is a highly organized tissue with closely packed parallel fibres aligned with the long axis of the tendon. The arrangement of the fibres makes the tissue almost uniaxial which allows the tendon to efficiently transfer tensile forces from muscle to bone. In unstretched tendons, the collagen fibres appear as wavy structures, called crimps (Franchi et al., 2007).

Tendons can be described as a composite of collagen fibres embedded in an extracellular matrix composed of proteoglycans, cells, elastin and water. Collagen makes up 65 - 80 % of the dry weight, mainly type I (O'Brien, 2005). The collagen molecules (tropocollagen) are organized into fibrils and held together and stabilized by chemical cross-links (Ker, 2007). Groups of parallel fibrils form a fibre, where a bundle of fibres constitute a fascicle, see figure 2. Fibrils and fibres are surrounded by endotenons, a loose connective tissue containing blood vessels, lymphatics and nerves. Groups of fascicles are bound by a similar connective tissue, called the epitenon, to form a tendon unit (Wang, 2006). The outermost layer is called the paratenon, which is a loose fatty tissue that reduce friction again surrounding tissue (Wang, 2006; O'Brien, 2005).

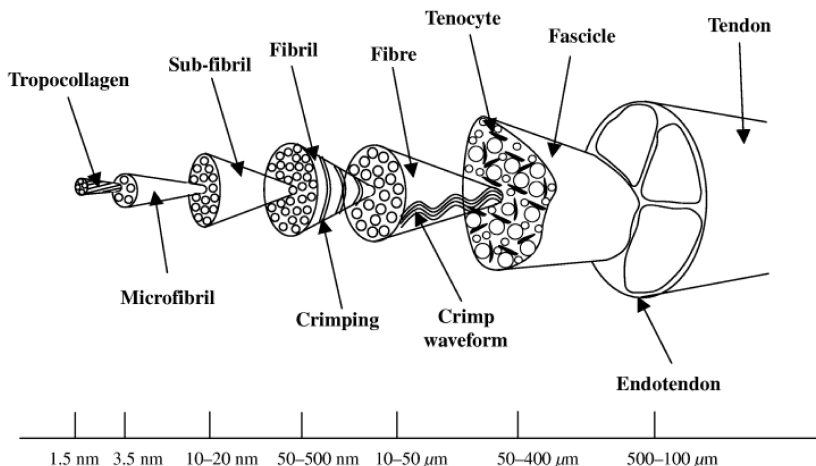Figure 2: Schematic picture of tendon, recreated from Ker, (2007).

The matrix is often referred to as the ground substance and 60 - 80 % of the wet weight is water. Less than 1 % of the tendon dry weight consists of proteoglycans. These compounds bind to the water molecules, giving the matrix a gel-like texture (O'Brien, 2005). The proteoglycans are orthogonally connected to the collagen fibrils, which

is believed to increase the tendon strength. They are probably also important for the orientation and ordering of the collagen fibrils (Franchi et al., 2007).

The cell density in tendons is low, and the cells are embedded in the extracellular matrix, aligned in rows in between the fibres. The cells are primarily tenoblasts and they synthesize the collagen molecules, proteoglycans and other proteins to build up the extracellular matrix (Wang, 2006). The cells are also functioning as sensors and adapt the extracellular matrix to changes in mechanical loading (Franchi et al., 2007).

2.1.1 Mechanical properties of tendons

A typical stress-strain curve from a tendon loaded in tension is shown in figure 3. For low strains, the stiffness is very low and this part of the curve is called the toe-region. When the tendon is subjected to load the crimps are stretched out, which corresponds to the toe-region in the load curve. When all the fibres are straightened, the load curve enters the linear region which corresponds to the physiological range of the tendon (Wang, 2006). For higher loads, the tendon starts suffering from microscopic failure where smaller fibril units rupture before the entire tendon breaks.
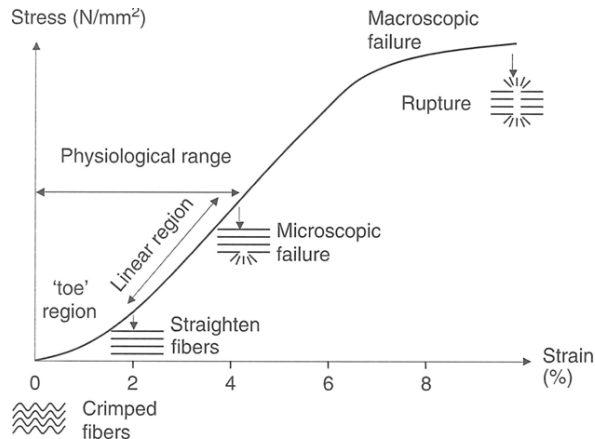

Figure 3: Schematic picture of stress-strain curve from tendon loaded in tension, from Wang, (2006).

The elastic modulus of tendons in adult vertebrates vary from 800 to 2000 MPa and tendons from animals that are not fully grown are generally less stiff (Ker, 2007). Tendons fail earlier under cyclic loading compared to static loading at the same level and time-to-rupture decreases with increased loading frequency (Ker, 2007). Tendons are highly anisotropic tissues. For example, mechanical testing of porcine tendons show that Youngs modulus is about 1000 times higher in the

fibre direction compared to the transverse direction (Von Forell et al., 2014).

Tendons are viscoelastic and their mechanical response is time dependent. If a tendon is subjected to a constant strain, the stress level will decease with time. This phenomenon is called stress-relaxation. Instead, if a constant load is applied, the sample length will increase with time. This is known as creep. Tendons exhibit creep for both static and cyclic loading (Ker, 2007). Both stress-relaxation and creep are illustrated in figure 4.
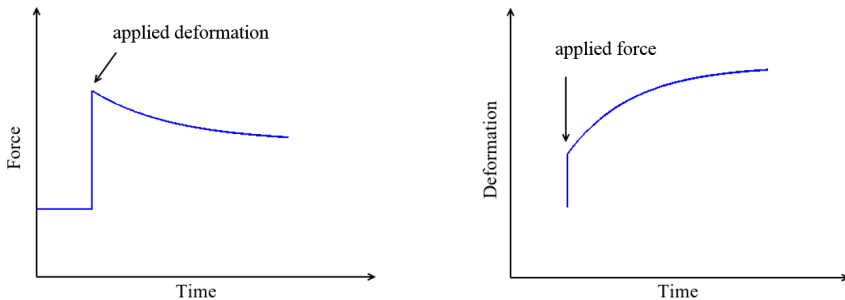

Figure 4: Stress-relaxation (left) and creep (right).

Moreover, the mechanical properties of tendons are strain rate dependent. At high strain rates the tendon stiffness is high and the tissue gets more brittle compared to lower strain rates where tendons are more compliant and absorb more energy (O'Brien, 2005).

The mechanisms behind stress-relaxation are not completely understood, but stress-relaxation tests on different length scales (on tendon fascicles, fibres and fibrils) show that stress-relaxation occur at different structural levels simultaneously. Fibers sliding relative each other is believed to be the major contributor to stress-relaxation (Gupta et al., 2010; Screen, 2008). The proteoglycan bonds in between fibre units at different levels and their tendency to break are therefore assumed to be important for the stress-relaxation response. As most of the stress-relaxation was noted as fibre gliding, these bonds may not be as strong as those at smaller length-scales (Screen, 2008). Stress-relaxation tests done in the transverse direction show that relaxation occur also in the ground substance and that the non-fibrillar matrix thereby also contribute to the viscoelastic behaviour of tendons (Yamamoto et al., 2000).

Creep in tendons is believed to be due to structural rearrangement and fibre recruitment that occur when tendons are loaded (Gupta et al., 2010). Tendons exhibit both primary and tertiary (accelerating) creep. In the primary creep stage, the strain rate is decreased with time until the tertiary creep begins and the strain rate increases radically. This is when the stiffness decreases and the tendon finally breaks (Ker, 2007).

Loading and unloading of viscoelastic materials follow different paths,

forming a loop in the stress-strain curve, see figure 5. The area formed inside the loop is called hysteresis and represents the energy loss. The hysteresis is sometimes given as percentage of energy loss between the loading and unloading curve. In tendons, the hysteresis is usually between 5-10% and the energy is lost as heat due to internal friction (Screen, 2008).
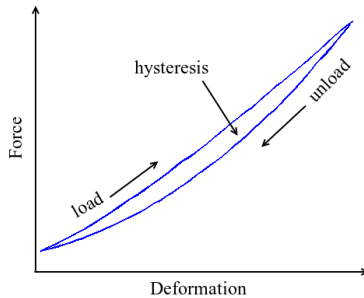

Figure 5: Hysteresis

2.2 Constitutive models for soft fibrous tissues

There is a variety of different models that have been used for modelling biological soft tissues and the choice of model depends on what biological and mechanical features that are investigated. There are two main types of models used for soft tissues: the continuum models and the structural models. In the continuum approach the material models are applied on tissue level while in the structural models the tissue properties are determined by the mechanical properties, structures and interactions of the different components (Lanir, 1979).

2.2.1 Continuum approach

The simplest model is Hooke's linear elastic model that can be used to describe isotropic or anisotropic linear materials (Korhonen and Saarakkala, 2011). This model is only valid for small strains and it is often insufficient when it comes to modelling biological soft tissues as they are subjected to large deformations.

Another group of materials are the hyperelastic materials with a non-linear stress-strain relationship appropriate for modelling large deformations. There are several different hyperelastic material models, e.g. the Neo-Hookean material and Moonely-Rivlin (Korhonen and Saarakkala, 2011). A hyper-elastic formulation was used to model the human Achilles tendon during running (Anitas and Lucaciu, 2013). Even if hyperelastic models can handle large deformations, they still

provide a simplified picture of tendons acting as nonlinear springs without taking the viscoelastic properties into consideration.

To capture the viscoelastic features of tendons (creep, stress relaxation and hysteresis), time-dependency needs to be included in the material model (Bergström and Boyce, 2001). This can be done by introducing viscous components, such as dash pots, and combine them with elastic springs. There are three classic viscoelastic solid material models; Maxwell, Kelvin-Voigt and the standard linear solid (SLS) model (Korhonen and Saarakkala, 2011). These can be combined to form more complex models.

The quasi-linear viscoelastic (QLV) theory was developed by Fung in the 60's and it has been used with success for tendons and ligaments (Screen, 2008). It is based on linear viscoelasticity, where a Boltzmann integral can be used to describe stress-relaxation. The time-dependent stress is calculated as a convolution of a relaxation function, $E(t)$, and strain ε, given in equation (1).

$$\sigma(t) = \int_0^t E(t - \tau) \frac{d\varepsilon(\tau)}{d\tau} d\tau \tag{1}$$

These models are called phenomenological, as pure mathematical functions are used to describe a certain behaviour. In quasi-linear viscoelasticity the relaxation function is separable and both time and strain dependent, $E(t, \varepsilon) = E_t(t)g(\varepsilon)$. The QLV model has been criticized as it predicts the rate of stress-relaxation to be independent of strain (Provenzano and Lakes, 2001; Davis and De Vita, 2012). Several models have been proposed to improve this shortcoming, for example by introducing non-separable relaxation functions (Davis and De Vita, 2012).

An important feature of soft tissues is the high water content. Poroelastic or biphasic models are used to describe a porous solid saturated with fluid. The basic idea is that the total stress in the tissue is a sum of the stresses from the solid matrix and from the fluid flow

$$\boldsymbol{\sigma}_{tot} = \boldsymbol{\sigma}_s + \boldsymbol{\sigma}_f = \boldsymbol{\sigma}_s - p\mathbf{I} \tag{2}$$

where p is the fluid pressure, $\mathbf{I}$ the unit tensor and $\boldsymbol{\sigma}_s$ is the stresses in the solid (Korhonen and Saarakkala, 2011). The frictional drag caused by the fluid flow gives the models a viscoelastic, time-dependent behaviour. As a result, the models will predict stress-relaxation if subjected to constant strain (Mak et al., 1987). The friction depends on the permeability of the solid matrix. For poroelastic models, Darcy's law

$$q = -k\nabla p \tag{3}$$

relates the fluid flow q to the permeability k and the pore pressure gradient ∇p. The permeability k can be defined as strain-dependent and isotropic or transversely isotropic. Apart from the equations describing the flow, a constitutive model describing the solid matrix is needed. For biphasic models, the governing equations look slightly different, but the idea is the same.

An advantage with these models is that they can be used to describe fluid flow and fluid velocities, in contrast to the previously described viscoelastic models. They are also more accurate in predicting local stresses, which is interesting when simulating failure and damage (Freutel et al., 2014).

Biphasic models have been widely used to model articular cartilage (Mak et al., 1987; Wilson et al., 2004; Julkunen et al., 2008) but the models have not been frequently used for modelling tendon behaviour. However, there is one example where stress-relaxation of mouse tail fascicles was quite successfully modelled with a biphasic, transversely isotropic model (Yin and Elliott, 2004). The solid matrix was assumed to be piecewise linear so that strain dependent parameters (elastic modulus in fibre direction E_3 and permeability k) had to be calculated in each strain increment. The disadvantage with the piecewise linear approach was that it did not provide globally valid parameters.

2.2.2 Structural approach

Some of the first structural models describing tendons contained a system of wavy collagen fibres that were attached to straight elastin fibres at numerous points. All constituents were assumed to be linear elastic. The model prediction agreed well with experimental data, but was only tested in tension (Lanir, 1978). The model was further developed for modelling skin where the fibre distribution and geometrical structure were found to be the reason for anisotropy and non-linear behaviour in the tissue (Lanir, 1979).

One important group of structural models are the fibre-reinforced models where fibres and ground substance are handled separately. By splitting the solid matrix into a fibrillar and a non-fibrillar part different constitutive models can be used for the different components. The stress in the solid matrix is then given by

$$\boldsymbol{\sigma}_s = \boldsymbol{\sigma}_{nonfibril} + \boldsymbol{\sigma}_{fibril} \qquad (4)$$

Fibre-reinforcement can also be included in the biphasic framework by combining equations (4) and (2), giving the total stress as

$$\boldsymbol{\sigma}_{tot} = \boldsymbol{\sigma}_{nonfibril} + \boldsymbol{\sigma}_{fibril} - p\mathbf{I} \qquad (5)$$

The main advantage of these models is that they represent all the main components in soft fibrous tissue (ground substance, collagen fibres and water) so that they can be used to investigate the structure, function and importance of each of them.

There are just a few structural models developed for tendons (Sverdlik and Lanir, 2002; Einat and Lanir, 2009). In these models, collagen fibres are considered to be the only load-bearing structures and contributions from the matrix and the fluid flow are neglected. So far, fibre-reinforced structural models have mainly been used to model articular cartilage (Wilson et al., 2004; Julkunen et al., 2008). The research

group where this thesis work is carried out has earlier started to implement the model developed by Wilson and Julkunen to tendons in a simplified unpublished work. In this project, a biphasic fibre-reinforced structural model is proposed for the Achilles tendon, considering both fibres, ground substance and fluid flow. It is the first structural model applied to the Achilles tendon, the largest tendon in the body.

2.2.3 Biphasic fibre-reinforced structural models

A previously published model for articular cartilage consisted of a biphasic, linear elastic solid matrix reinforced with viscoelastic fibres (Wilson et al., 2004). The fibres consisted of large primary fibres, arranged in an archade like formation, and secondary smaller fibres randomly distributed. All collagen fibres were assumed to be one dimensional, viscoelastic structures that only could carry load in tension (Wilson et al., 2004). The fibres were represented by unit vectors, $\mathbf{e}_f$, that described the current direction of the fibres. Since the fibres underwent large deformations, logarithmic strain was used to calculate the strains in the fibres

$$\varepsilon_f = log(\lambda) \tag{6}$$

where λ is the fibre stretch, calculated as the ratio between the current and initial fibre length $\mathbf{e}_{f,0}$

$$\lambda = \frac{|\mathbf{e}_f|}{|\mathbf{e}_{f,0}|} \tag{7}$$

A standard linear solid model was used to capture the viscoelastic features, see figure 6, where a linear spring was used parallel with a non-linear spring and a dashpot in series (Wilson et al., 2004, 2005b). Later, exponential functions were used to include a non-linear stress
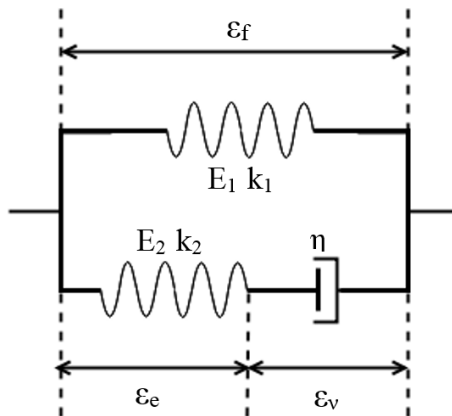

Figure 6: Schematic figure of the standard linear solid model

strain relationship in the springs (Wilson et al., 2006). Due to the large deformations, the stresses were expressed as the first Piola-Kirchoff stress P

$$P_1 = E_1 \left(e^{k_1 \varepsilon_f} - 1\right) \quad for \quad \varepsilon_f > 0 \tag{8}$$
$$P_1 = 0 \quad for \quad \varepsilon_f \le 0$$

and

$$P_2 = E_2 \left(e^{k_2 \varepsilon_e} - 1\right) \quad for \quad \varepsilon_e > 0 \tag{9}$$
$$P_2 = 0 \quad for \quad \varepsilon_e \le 0$$

where the stress is zero for zero strain, to ensure that the fibres only carry load in tension. The total fibre stress was

$$P_f = P_1 + P_2 \tag{10}$$

As the first Piola-Kirchoff stress always is calculated with respect to the reference configuration and the Cauchy stress $\boldsymbol{\sigma}_f$ is calculated with respect to the current configuration the following transformation was used

$$\boldsymbol{\sigma}_f = \frac{\lambda}{J} P_f \mathbf{e}_f \mathbf{e}_f^T \tag{11}$$

where J is the Jacobian of the deformation tensor $\mathbf{F}$. A complete derivation of the equations can be found in Wilson et al. (2006).

The main advantage with the exponential formulation was that the collagen stiffness was strain dependent (Wilson et al., 2006), unlike the first versions where the collagen stiffness was assumed to be strain-independent (Wilson et al., 2004).

Even the model for the non-fibrillar part of the matrix was further developed to include large deformations. The solid matrix was assumed to be compressible and modelled with a neo-Hookean (hyperelastic) formulation (Wilson et al., 2005a). The energy function (van Loon et al., 2003; Krenk, 2009) was

$$W_{nf} = \frac{K_m}{2} \left(\frac{1}{2}(J^2 - 1) - ln(J)\right) + \frac{1}{2}G_m \left(tr(\mathbf{C}) - 3det(\mathbf{C})^{1/3}\right) \tag{12}$$

where the first part is the compressible part. J is the Jacobian of the deformation gradient and $\mathbf{C}$ the right Cauchy-Green tensor. The bulk modulus K_m is defined as

$$K_m = \frac{E_m}{3(1 - 2\nu_m)} \tag{13}$$

and the shear modulus G_m is defined as

$$G_m = \frac{E_m}{2(1 + \nu_m)} \tag{14}$$

where E_m is Young's modulus of the matrix and ν_m is Poisson's ratio. The Cauchy stress in the matrix was given by

$$\boldsymbol{\sigma}_{nf} = \frac{K_m}{2} \left(J - \frac{1}{J}\right) I + \frac{G_m}{J} \left(\mathbf{B} - J^{2/3}I\right) \tag{15}$$

where $\mathbf{B}$ is the left Cauchy-Green tensor.

The permeability, k, was assumed to be strain-dependent and was given by

$$k = k_0 \left(\frac{1 + e}{1 + e_0} \right)^{M_k} \tag{16}$$

where k_0 is the initial permeability, M_k a positive constant and e and e_0 the current and initial void ratios (Wilson et al., 2004). The void ratio in a porous medium is defined as the volume ratio between fluid and solid

$$e = \frac{n_f}{n_s} \tag{17}$$

The total water volume fraction, n_f, was estimated from the water mass fraction $n_{f,m}$ (Julkunen et al., 2008) as

$$n_f = \frac{\rho_s n_{f,m}}{1 - n_{f,m} + n_{f,m}\rho_s} \tag{18}$$

where ρ_s is the assumed solid tissue density.

2.3 Mechanical testing of rat Achilles tendons

To evaluate if this mechanical model can capture the behaviour of the Achilles tendon, it is important to compare its behaviour to well-controlled experimental data. This was obtained from collaborators (Eliasson et al., 2007) from a study where Achilles tendons from rats were tested under cyclic loading. Two groups from the study are used in this project. The first data set consists of nine tendons from 16 weeks old normal rats, forming the control group in the study. These rats had intact Achilles tendons that were loaded as normal under daily activity. The second data set is from a group of twelve 10 weeks old rats that had botulinum toxin injected in their calf muscles to unload the Achilles tendon through muscle paralysis. This is a common model in rats that is used for hindlimb unloading. The tendons were harvested and tested one or six weeks after the injection (Eliasson et al., 2007). Only tendons from week six are used as references for the computational model.

The tendons were harvested together with the calcaneal bone, figure 1, and kept moist with physiological solution during the entire sample preparation. The muscles were scraped off the tendon end that was clamped between sandpaper to avoid sliding. In the other end, the bone was fixed in a clamp. The mechanical test were realized with a testing machine (100R, DDL, Eden Praire, MN) that pulled at a constant speed of 0.1 mm/s. Load control was used to subject the samples to cyclic loading. The tendons were loaded from 1 to 20 N for 20 cycles.

The three first load cycles from the control group (specimen 1265 - 1277) are showed in figure 7 and from the paralysed group (specimen 1209 - 1247) in figure 8. The results from both groups show great variability over time and very distinct toe regions. In figure 7 and 8, two extreme samples are marked with colour and the remaining samples are found in between.
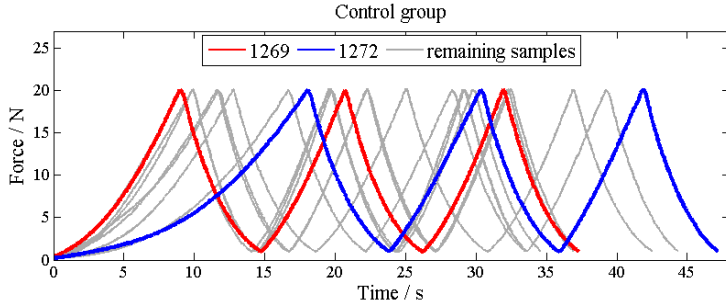
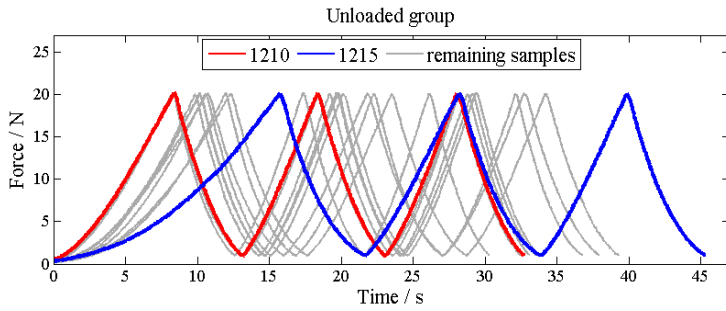Figure 7: Force vs time for the control group, specimen number 1265 - 1277.

Figure 8: Force vs time for the paralysed group, specimen number 1209 - 1247.

In the study, the unloaded lengths and cross-sectional areas of all specimens were measured, see Appendix A. Moreover, elastic modulus, stiffness, peak force, peak stress and hysteresis were measured from the mechanical testing. The results showed that creep and hysteresis were significantly decreased in the paralysed group compared to the control group and that the modulus was increased (Eliasson et al., 2007).

3 Methods

3.1 Constitutive model for the Achilles tendon

The constitutive model for the Achilles tendon is based on the model described in section 2.2.3, previously used to model articular cartilage. The Achilles tendon is assumed to be biphasic and the porous solid phase is fully saturated with water. The non-fibrillar matrix is modelled with a compressible and isotropic neo-Hookean material given by the energy potential W in equation (12). The Cauchy stress is derived from the energy potential as

$$\boldsymbol{\sigma}_{nf} = \frac{2}{J}\mathbf{F}\frac{\partial W}{\partial \mathbf{C}}\mathbf{F}^T \tag{19}$$

where the full derivation can be found in Appendix B. The collagen fibres are assumed to run parallel with the long axis all through the tendon and only primary fibres are considered.

The viscoelastic collagen fibres are modelled with the standard linear solid (SLS) model pictured in figure 6, where a spring is connected in parallel to a Maxwell element (a spring and a dash pot connected in series). Two different versions of the collagen model are derived, first with linear elastic springs and then for springs with an exponential stress-strain relationship. E_1 and E_2 are the spring stiffnesses, where the subscript 1 corresponds to the spring connected in parallel with the Maxwell element, see figure 6, η is the damping constant and k_1 and k_2 are two additional spring constants for the exponential model. The total fibre strain is denoted ε_f, ε_e is the strain in spring 2 and ε_ν is the strain in the dash pot.

3.1.1 Standard linear solid model with linear springs

In the linear model, the stress in spring 1 is

$$\sigma_1 = E_1\varepsilon_f \tag{20}$$

The stress in the Maxwell element equals the stress in spring 2 or the stress in the dash pot

$$\sigma_2 = E_2\varepsilon_e = \eta\dot{\varepsilon}_\nu \tag{21}$$

The fibre strain equals the sum of the strains in spring 2 and the dash pot

$$\varepsilon_f = \varepsilon_e + \varepsilon_\nu \tag{22}$$

and the total stress of the entire system is the sum of the two parallel systems

$$\sigma_f = \sigma_1 + \sigma_2 \tag{23}$$

Inserting equations (20) and (21) into equation (23) results in

$$\sigma_f = E_1\varepsilon_f + \eta\left(\dot{\varepsilon}_f - \dot{\varepsilon}_e\right) = E_1\varepsilon_f + \eta\left(\dot{\varepsilon}_f - \frac{\dot{\sigma}_2}{E_2}\right) \tag{24}$$

$$\sigma_f = E_1 \varepsilon_f + \eta \left(\dot{\varepsilon}_f - \frac{(\dot{\sigma}_f - E_1 \dot{\varepsilon}_f)}{E_2} \right) \tag{25}$$

$$\sigma_f + \frac{\eta}{E_2} \dot{\sigma}_f = E_1 \varepsilon_f + \eta \dot{\varepsilon}_f + \frac{\eta E_1}{E_2} \dot{\varepsilon}_f \tag{26}$$

Time integration of (26) with an Euler backward step gives

$$\sigma_f^{t+\Delta t} + \frac{\eta}{E_2} \left(\frac{\sigma_f^{t+\Delta t} - \sigma_f^t}{\Delta t} \right) = E_1 \varepsilon_f^{t+\Delta t} + \left(\eta + \frac{\eta E_1}{E_2} \right) \left(\frac{\varepsilon_f^{t+\Delta t} - \varepsilon_f^t}{\Delta t} \right) \tag{27}$$

and the total stress can be expressed as

$$\sigma_f^{t+\Delta t} = \frac{\left(\sigma_f^t \frac{\eta}{\Delta t E_2} + \left(E_1 + \frac{\eta}{\Delta t} + \frac{\eta E_1}{\Delta t E_2} \right) \varepsilon_f^{t+\Delta t} - \left(\frac{\eta}{\Delta t} + \frac{\eta E_1}{\Delta t E_2} \right) \varepsilon_f^t \right)}{\left(1 + \frac{\eta}{\Delta t E_2} \right)} \tag{28}$$

3.1.2 Standard linear solid model with exponential springs

The derivation of the equations describing the SLS model with exponential springs follow the same procedure as for the linear model in the previous section. The exponential stress-strain relationships in equation (8) and (9) are repeated here

$$P_1 = E_1 \left(e^{k_1 \varepsilon_f} - 1 \right) \tag{29}$$

$$P_2 = E_2 \left(e^{k_2 \varepsilon_e} - 1 \right) = \eta \dot{\varepsilon}_\nu \tag{30}$$

The total stress is the sum of the two parallel systems

$$P_f = P_1 + P_2 \tag{31}$$

The following relationships are used below when deriving the stresses

$$\varepsilon_e = \frac{1}{k_2} \ln \left(\frac{P_2}{E_2} + 1 \right) \tag{32}$$

$$\dot{\varepsilon}_e = \frac{\dot{P}_2}{k_2 (P_2 + E_2)} \tag{33}$$

Inserting equation (22) into equation (31) gives

$$P_f = P_1 + P_2 = P_1 + \eta \left(\dot{\varepsilon}_f - \dot{\varepsilon}_e \right) \tag{34}$$

and with the use of equations (33) and (31) the stress P_f can be expressed as a function of ε_f only

$$P_f = P_1 + \eta \left(\dot{\varepsilon}_f - \frac{\dot{P}_2}{k_2 (P_2 + E_2)} \right) = P_1 + \eta \left(\dot{\varepsilon}_f - \frac{\dot{P}_f - \dot{P}_1}{k_2 (P_f - P_1 + E_2)} \right) \tag{35}$$

14

Some rearrangements give the quadratic equation

$$P_f^2 + P_f(E_2 - 2P_1 - \eta\dot{\varepsilon}_f) + \frac{\eta}{k_2}\dot{P}_f - (P_1 + \eta\dot{\varepsilon}_f)(E_2 - P_1) - \frac{\eta}{k_2}\dot{P}_1 = 0 \quad (36)$$

and time integration with an Euler backward step results in

$$\left(P_f^{t+\Delta t}\right)^2 + P_f^{t+\Delta t}\left(E_2 - 2P_1 - \eta\dot{\varepsilon}_f + \frac{\eta}{k_2\Delta t}\right) \quad (37)$$

$$-\frac{\eta}{k_2\Delta t}P_f^t - (P_1 + \eta\dot{\varepsilon}_f)(E_2 - P_1) - \frac{\eta}{k_2}\dot{P}_1 = 0$$

where

$$\dot{\varepsilon}_f = \frac{\varepsilon_f^{t+\Delta t} - \varepsilon_f^t}{\Delta t} \quad (38)$$

and

$$\dot{P}_1 = E_1 k_1 e^{k_1\varepsilon_f}\dot{\varepsilon}_f \quad (39)$$

Finally, this can be written as a quadratic equation on standard format

$$\left(P_f^{t+\Delta t}\right)^2 + bP_f^{t+\Delta t} + c = 0 \quad (40)$$

where

$$b = E_2 - 2P_1 - \eta\dot{\varepsilon}_f + \frac{\eta}{k_2\Delta t} \quad (41)$$

$$c = -\frac{\eta}{k_2\Delta t}P_f^t - (P_1 + \eta\dot{\varepsilon}_f)(E_2 - P_1) - \frac{\eta}{k_2}\dot{P}_1 \quad (42)$$

The total stress is found as the positive root of equation (40)

$$P_f^{t+\Delta t} = -\frac{b}{2} + \frac{1}{2}\sqrt{b^2 - 4c} \quad (43)$$

3.2 Finite element implementation and optimization

3.2.1 Average tendon

Due to the large variations in both geometry and load response in both groups, it was of intrerest to create an average tendon representing each group. It was not possible to just take the average of all data, due to the large spreading over time, see figures 7 and 8. A reasonable average tendon must have the same strain rate as the samples, 0.1 mm/s and the load cycles must vary between 1 and 20 N. To meet these requirements, the cyclic loading was transformed to the frequency domain, by interpolating the force values for each cycle over 2π, see figure 9 and 10. Then the average force could be calculated for each cycle. To transform the average force vector back to the time domain, the force in each load cycle was interpolated over the corresponding average period (time duration for one cycle). The same procedure was used to take the average of the displacements.
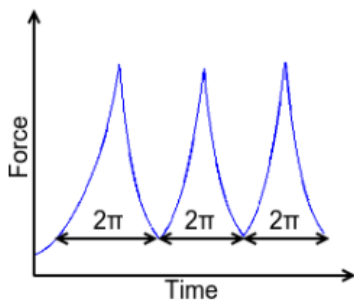
Figure 9: Force vs time. To transform the force to the frequency domain each load cycle must be interpolated over 2π.
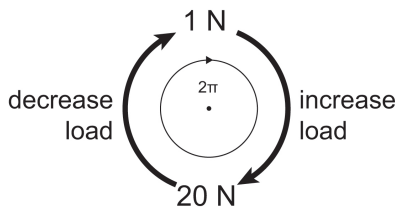

Figure 10: Schematic picture of cyclic loading showing that one cycle equals 2π.

The average tendons from the control and paralysed group are shown in figure 11 and 12 respectively. The red lines show the created average tendons and the grey lines are all the samples from the corresponding group. The shapes of the average tendon force curves are consistent with the experimental data and they appear to give a reasonable average description of each group.
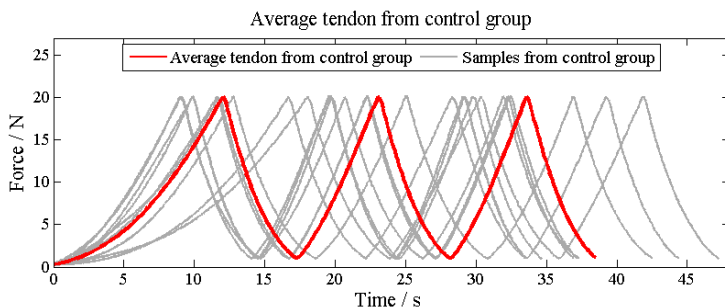

Figure 11: Force-time relationship for the created average tendon from the control group (red line) together with all the control samples (grey lines).

Average unstretched geometries were created by taking the mean values of the lengths and radii in each group, see Appendix A. The dimensions for the average tendon from the control group were 8.74 mm by 0.695 mm and the corresponding values for the average tendon from the paralysed group were 8.51 mm by 0.730 mm.
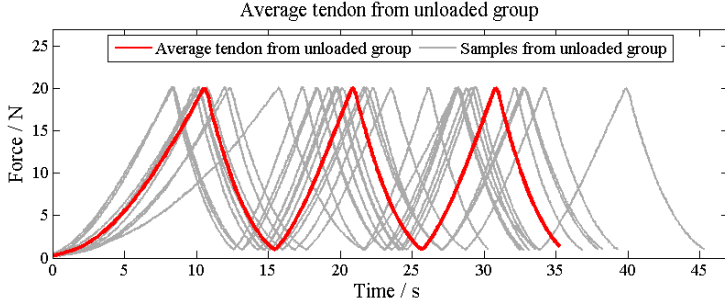
Figure 12: Force-time relationship for the created average tendon from the paralysed group (red line) together with all the samples from the paralysed group (grey lines).

3.2.2 Geometry and mesh

Sample specific finite element models were created for all specimens (9 from the control group, 12 from the paralysed group and one average sample for each group) based on the length and cross-section area of each sample.

To reduce the computational cost, the cross-sectional area was assumed to be circular and quadratic, axisymmetric, poroelastic elements, CAX4P, were used. With axisymmetric elements the cylindrical domain is reduced to a rectangle, with the same height as the cylinder and the width of the radius. The rectangle is cut out from the cylinder at an angle that equals zero, see figure 13. All elements and nodes on the rectangle then represents the circle that is created if the element or node is rotated 360° around the z-axis. In this way, a 3D geometry can be represented by a 2D domain.

The mesh size was chosen so that there were four elements in each row to simplify the coding and the average mesh size was 0.18 mm. The number of elements varied between 180 and 236 elements, depending on the size of the geometry and a mesh dependency study was carried out to check that the number of elements was sufficient. An example of a mesh is shown in figure 13. A complete list of the sample geometries and meshes is found in Appendix A.

3.2.3 Boundary conditions

A schematic picture of the boundary conditions is shown in figure 13. The bottom side of the domain was clamped and the nodes on the z-axis were fixed in the radial direction. The pore pressure was set to zero at the right edge.

Displacement controlled loading was used in the numerical calculations, mimicking the experimental data during the first three load cycles. The loading scenario was divided into seven steps, first a preload and then six steps with loading and unloading corresponding to three
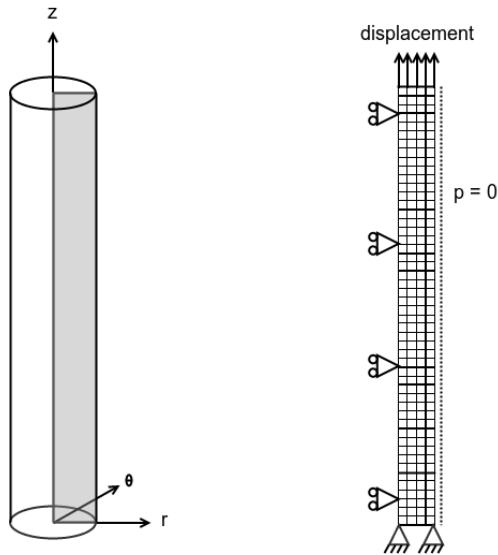
Figure 13: The rectangular 2D domain is marked with grey inside the cylinder (left) and a typical mesh with applied boundary conditions (right).

whole cycles. The loading time for each step was determined by finding maximums and minimums in the time-displacement curve from the experiments, see figure 14. This was done with the function `findpeaks` in Matlab. The time for the preload was calculated based on the displacement at time zero divided by 0.1 mm/s.
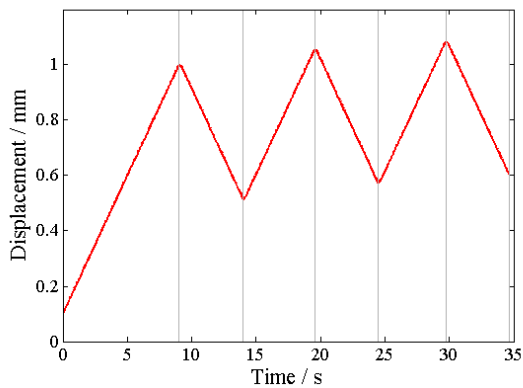

Figure 14: Time-displacement curve from mechanical testing used to determine the time intervals and displacements for each step.

3.2.4 Porosity

The tendon dry weight from the experimental study was 19 mg, the water content 63 mg and the water mass fraction 76 % (Eliasson et al., 2007). The assumed solid tissue density is calculated as the fraction of dry weight and volume (Appendix A), $\rho_s = 1.4 g/ml$. The total water volume fraction is calculated with equation (18) to be 0.82.

3.2.5 Numerical implementation

The finite element model was implemented in Abaqus (v6.12-4, Dassault Systems, France). A subroutine for user-defined materials (UMAT) was used to define the material model of the solid matrix (ground substance and collagen fibres) described in section 3.1.

To account for the large deformations an updated Lagrangian formulation was used. The updated Lagrangian formulation is appropriate for large deformations as the reference configuration $\mathbf{x}^n$ is continuously updated instead of keeping the initial configuration $\mathbf{x}^0$ as reference throughout the calculations. With the updated Lagrange scheme, the deformation gradient is defined as

$$F = \frac{\partial \mathbf{x}^{n+1}}{\partial \mathbf{x}^n} \tag{44}$$

where $\mathbf{x}^n$ is a line element in the last converged iteration n and $\mathbf{x}^{n+1}$ the current deformed state. The equivalence in one dimension is the stretch

$$\lambda = \frac{dx^{n+1}}{dx^n} \tag{45}$$

In Abaqus, the updated Lagrangian formulation was specified in the input file with the keyword `NLGEOM` (geometric non-linearities). For the subroutine to be consistent with the functions in Abaqus, the same updated formulation had to be used in UMAT (user defined material) for the fibre stretch.

The fibres were represented by direction vectors, where $\mathbf{e}^n$ corresponds to the reference configuration and $\mathbf{e}^{n+1}$ the deformed configuration. The fibre stretch was defined as the length ratio between the direction vectors

$$\lambda = \frac{|\mathbf{e}^{n+1}|}{|\mathbf{e}^n|} \tag{46}$$

The strain increment was calculated as the logarithmic strain from the stretch

$$\Delta\varepsilon = ln\left(\frac{|\mathbf{e}^{n+1}|}{|\mathbf{e}^n|}\right) = ln\left(\lambda\right) \tag{47}$$

and the total strain in increment $n + 1$ was

$$\varepsilon^{n+1} = \varepsilon^n + \Delta\varepsilon \tag{48}$$

In each iteration the fibre direction vectors had to be updated and the deformed direction vectors were calculated from the deformation gradient as

$$\mathbf{e}^{n+1} = \mathbf{F}\mathbf{e}^n \tag{49}$$

3.2.6 Note on permeability

The concept of permeability can easily lead to confusion when turning to literature, as there are three slightly different parameters that all are called permeability. The first one, denoted K, is often used in biomechanical literature and has the unit $[m^4/(Ns)]$. The second one, $\hat{k}$, with unit $[m^2]$, is sometimes called intrinsic permeability as it only depends on the solid matrix and not on the fluid phase. Finally, there is k, also called hydraulic conductivity, with unit $[m/s]$. This is the parameter used in Darcy's law in ABAQUS and further on the word permeability refers to this parameter k. The following conversion formula holds

$$k = \frac{\hat{k}\rho g}{\mu} = K\rho g \tag{50}$$

where μ is the fluid viscosity, ρ the fluid density and g is the standard gravity.

3.3 Optimization

The mechanical model was fitted to experimental data by optimizing nine parameters $(E_1, E_2, k_1, k_2, \eta, k_0, M_k, E_m, \nu_m)$. A schematic picture of the curve fitting procedure is shown in figure 15. The objective function, $o(\mathbf{p}) = min(\mathbf{f})$ in figure 15, was the minimum of the mean squared error between experimental and simulated reaction forces, see equation (51). The curves were locally optimized for each of the six load steps (the preload was excluded from the optimization) by calculating the mean squared errors separately. All steps were weighted equally and averaged, see equation (51) (Heuijerjans, 2012).

$$f = \frac{1}{6}\sum_{i=1}^{6}\frac{1}{n_i}\left(\sum_{j=1}^{n_i}((F_{mod})_j - (F_{exp})_j)^2\right) \tag{51}$$

F_{mod} is the simulated reaction force, F_{exp} is the experimental reaction force and n_i the number of data points in each load step. A non-linear unconstrained optimization algorithm (`fminsearch`) in Matlab was used to minimize (51), starting from an initial guess.

The fitting procedure was iterative and in every iteration step in the optimization Abaqus was called from within Matlab so that a new finite element simulation was run with updated material parameters. The optimization stopped when the convergence criteria, given as numerical tolerances, were fulfilled or when it reached the maximum number of 2000 iterations. The tolerances for the optimization algorithm were
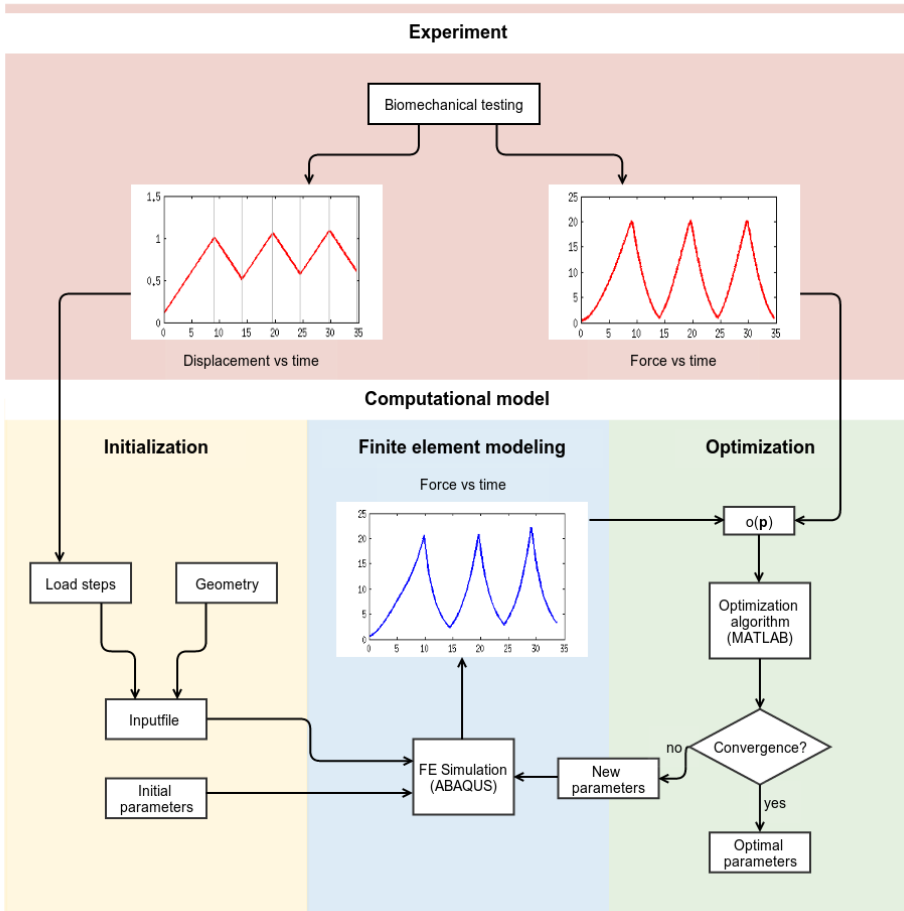
Figure 15: Flow chart of the curve fitting procedure.

specified using the `optimset` function. Both the tolerance on the objective function (TolFun) and the step size tolerance (TolX) was set to 10^{-5}.

Non-linear finite element simulations in Abaqus also involve iterative processes and for the optimization to function the finite element simulations had to converge. The minimum allowed time step in Abaqus was set to 10^{-5} seconds. The convergence in Abaqus depended heavily on the material parameters in the initial guess. Therefore, finite element simulations were run for different initial parameters beforehand, to find good starting points for the optimization. All optimizations were run several times with different initial values to avoid bad fits corresponding to local minima.

Finally, the curve fits from the optimizations were evaluated by taking the root mean square (RMS) of the differences between the reaction

force from the model, F_{mod}, and the experiment, F_{exp}, at n data points

$$RMS = \sqrt{\frac{\sum_{i=1}^{n} \left((F_{mod})_i - (F_{exp})_i \right)^2}{n}} \qquad (52)$$

The RMS is a standard method for evaluating curve fits and equation (52) is a measure of the global fit, as opposed to equation (51) where the errors are calculated locally.

4 Results

The suggested model with an exponential stress-strain relationship for the collagen was able to accurately capture the mechanical behaviour of rat Achilles tendons subjected to cyclic loading, while the model with linear spring was found to be inadequate to describe these large deformations. Figure 16 show one curve fit done with linear springs on sample 1267. It is clear that the strict exponential behaviour of the load curve could not be captured with the linear springs. For this reason, the linear springs were abandoned in favour of the springs with exponential stress-strain relationship.
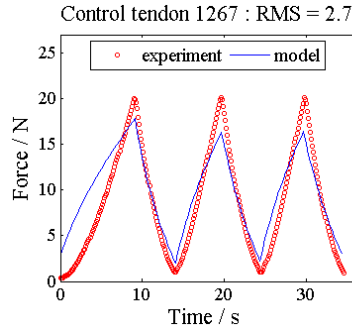

Figure 16: Curve fit with SLS model with linear springs.

The nine material parameters in the exponential model was fitted to 21 samples (9 from the control group and 12 from the paralysed group) and two additional average tendons. The overall fit was good for all samples with root mean square errors (RMS) between 0.66 and 1.2. The curve fit for the average tendon from the control group is shown in figure 17 and the result for the average paralysed tendon is shown in figure 18. The remaining curve fit plots are found in Appendix C.
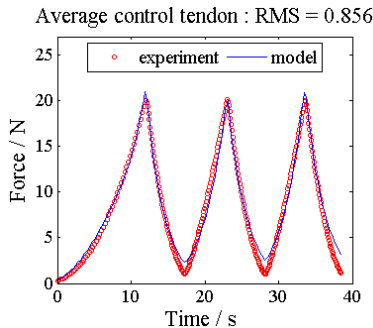

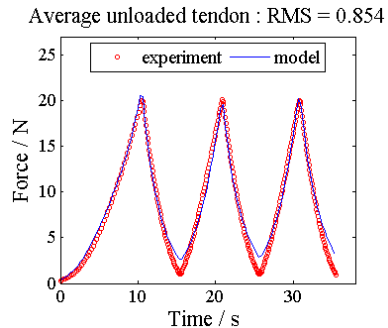Figure 17: Curve fit of the average tendon from the control group. RMS = 0.856

Figure 18: Curve fit of the average tendon from the paralysed group. RMS = 0.854

There are a few regions in the loading curves where the model predictions are inferior, namely the toe-region and the extreme points of the loading curve. In general, the fit in the toe region was worse for those samples with a long first load step. The model predicted the force at the end of the unloading steps to be slightly too high in almost all samples. There were also overshoots at the force peaks, mainly in the first and third loading. The average error was 5% at the force peaks and the worst prediction was approximately 13 % too high.

The material parameters from the optimizations of control tendons are presented in table 1 and those of paralysed tendons in table 2. The mean values in the tables are the mean parameter values of all tendons in each group and SD is the corresponding standard deviation. Tendon_1 is the average tendon created based on the control group and Tendon_2 is the average tendon created based on the paralysed group.

An analysis of the material parameters with a students t-test showed that there are no significant differences between the two groups. There are large variations in the optimized parameters, which reflect the variability in the data, see figure 11 and 12.

Table 1: Parameters from optimization of tendons from control group.

sample	RMS	E_1 (MPa)	E_2 (MPa)	k_1	k_2	η (MPa s)	k_0^* (mm/s)	M_k	E_m (MPa)	ν_m
1265	0.724	0.038	0.145	32.5	35.7	364.3	1.39E-09	0.82	0.75	0.31
1267	0.877	0.143	0.351	38.0	44.3	863.6	1.28E-09	1.27	0.98	0.31
1268	0.963	0.041	0.325	37.3	41.2	417.7	1.05E-07	0.61	1.12	0.37
1269	0.659	0.425	0.327	28.2	41.8	399.8	1.00E-07	0.68	1.09	0.18
1270	0.952	0.052	0.107	40.5	51.8	765.9	1.00E-07	0.67	1.62	0.27
1272	1.166	0.006	0.134	31.8	31.9	368.4	1.94E-10	1.01	1.00	0.30
1274	0.830	0.036	0.540	39.3	34.8	415.3	8.40E-12	1.22	0.93	0.30
1275	1.102	0.009	0.112	32.9	36.3	358.0	9.67E-10	0.99	0.74	0.26
1277	0.865	0.069	0.312	34.6	41.1	481.9	1.00E-07	0.85	1.15	0.27
mean	-	0.091	0.261	35.0	39.9	492.8	4.55E-08	0.90	1.04	0.29
SD	-	0.13	0.15	4.04	6.00	187.97	5.30E-08	0.24	0.26	0.05
Tendon_1	0.856	0.031	0.396	37.0	32.4	482.9	9.37E-10	0.95	1.03	0.29

---

*The large spread in the permeability values is due to different initial parameters.

Table 2: Parameters from optimization of tendons from paralysed group.

sample	RMS	E_1 (MPa)	E_2 (MPa)	k_1	k_2	η (MPa s)	$k_0{}^*$ (mm/s)	M_k	E_m (MPa)	ν_m
1209	0.896	0.100	0.284	43.6	51.8	446.8	5.24E-08	1.28	0.57	0.31
1210	0.743	0.145	0.540	32.2	33.1	493.7	7.20E-08	0.40	1.12	0.19
1211	0.908	0.057	0.206	33.6	38.9	416.1	1.00E-07	0.96	1.01	0.30
1215	1.146	0.080	0.309	29.4	48.2	598.1	1.20E-09	1.04	0.99	0.32
1218	0.826	0.032	0.195	42.4	41.3	581.0	9.59E-08	0.98	0.96	0.30
1219	0.702	0.073	0.720	38.0	28.2	953.4	8.27E-08	1.33	0.57	0.34
1223	1.061	0.038	0.210	37.9	37.7	521.8	1.01E-09	1.01	1.02	0.31
1224	0.856	0.109	0.201	37.6	45.6	999.0	4.94E-08	0.29	0.70	0.03
1241	0.969	0.061	0.255	44.0	45.5	415.7	5.40E-08	1.75	0.60	0.20
1242	0.983	0.081	0.096	39.0	53.1	814.3	5.86E-09	1.39	0.98	0.05
1246	0.871	0.058	0.251	39.5	45.0	737.7	9.88E-08	0.99	1.06	0.27
1247	0.868	0.038	0.326	37.9	37.6	553.5	1.87E-09	0.31	0.71	0.38
mean	-	0.073	0.300	37.9	42.2	627.6	5.13E-08	0.98	0.86	0.25
SD	-	0.03	0.17	4.44	7.43	202.50	4.00E-08	0.45	0.21	0.11
Tendon$_2$	0.854	0.094	0.305	34.7	40.6	578.0	7.70E-10	0.92	0.93	0.33

5 Discussion

The proposed fibre-reinforced poroviscoelastic finite element model successfully predicted the overall response of the Achilles tendon subjected to cyclic loading. However, the model slightly over-estimated the reaction force in between the cycles and also sometimes incorrectly predicted the toe-region. There was a clear trade off between the fits in these areas, where a well pictured toe-region lead to worse predictions of the force levels at the dips and vice versa. Sample 1269, see figure 7, did not have a very pronounced toe-region which probably is the reason for why the fit is very good even at low forces, see figure 22. The mean values of the optimized parameters are slightly different from the optimized values for the average tendons, see table 1 and 2. This is not very surprising as there is a large variability among the samples which is also seen in the optimized parameters.

For viscoelastic materials, loading and unloading does not follow the same curve (hysteresis) and therefore it is important that a finite element model can capture this behaviour. In this project, three entire load cycles were used for the curve-fitting to make sure that both load types were captured accurately. Three cycles correspond to about 40 seconds and the simulations therefore also give a hint of the model's behaviour over time. Ideally, the model should work for a large number of consecutive cycles but due to computational costs and numerical instabilities three cycles were considered enough. Also, during the first load cycles the viscoelastic behaviour changes the most which is another reason for why the first three load cycles were used.

As the models used for tendons look very different, it is often difficult to compare material parameters with other studies. However, parts of the model or single parameters can still be compared. One study that is based on the Zener model (another name for the Standard Linear Solid model) and used for the Achilles tendon on rabbits found damping coefficients of 377.3 ± 88.7 MPa s (Kahn et al., 2013). Those values are of the same magnitude as the ones found in this study.

One main difference between this model and Kahn's model is the interpretation of the viscous model. In their case, the fibres are represented by a non-linear spring in parallel with a Maxwell element, containing one linear spring and one damper, representing the matrix. Thus, their entire model correspond to the collagen part in this model. It is not surprising that both models give accurate results, as the collagen fibres carry most of the load in this model, but it illustrates the difficulties in telling what biological feature each part of the model actually represents. As several studies show that individual collagen fibres show viscoelastic behaviour (Gupta et al., 2010; Gautieri et al., 2013) and transverse loading experiments report the matrix to be about 1000 times weaker than the fibres (Von Forell et al., 2014), it is reasonable to let the SLS-model represent the collagen fibres only and let a much weaker hyper-elastic material represent the matrix.

There are several ways used in literature to address the non-linearities

in the tendon stress-strain curve. One approach is to use different Young's modulus for the toe-region and the linear region. This is avoided in this model, as the exponential springs are able to capture the entire stress-strain curve with the same material parameters for all strains. E_1 and E_2 determine the shape of the curve for low strains. For example, by looking in table 1 and in figure 7, it is clear that tendons with a long toe-region (sample 1272 and 1275) have lower E_1. In one study, mouse tail fascicles were modelled with the following stress-strain relationship in the fibre direction: $\sigma = A(e^{B\varepsilon} - 1)$ (Yin and Elliott, 2004). That is very similar to the stress-strain relationship used for the non-linear springs in this model, $\sigma = E(e^{k\varepsilon} - 1)$. They reported $A = 1.06 \pm 1.31$ and $B = 28 \pm 12.5$ (Yin and Elliott, 2004). A is higher than $E_{1,2}$ and B is a bit lower than $k_{1,2}$, but the main feature with a small coefficient A and a higher exponent B is the same. It is not surprising that one value is higher and the other is lower as the resulting stiffness is a trade off between A and B.

Another approach is to use several linear Maxwell elements connected in parallel, but that easily leads to a high number of material parameters. One study modelled the Achilles tendon as a hyper-elastic material combined with seven Maxwell elements, which resulted in 17 different material parameters that had to be optimized to experimental data (Tang et al., 2011). However, it is probably wise to try to limit the number of material parameters, both as the optimization procedure gets more complicated and as it is more difficult to interpret the physical meaning of the constants. A draw back for the tendon model presented in this thesis, when it comes to the physical interpretation of the constants, is the use of springs with exponential stress-strain relationships that are not so easily visualized compared to linear elastic spring. However, the use of exponential stress-strain relationships makes it sufficient with nine constants in total, where each constant is easily related to a specific part of the model (collagen fibres, matrix or fluid).

Anisotropy is an important property of tendons. In this model, the anisotropic properties arise from the one dimensional parallel fibres. They give the tissue strength in the longitudinal direction but not in the transverse, where only the matrix carry load. Both the matrix and the permeability are assumed to be isotropic. For the matrix, this simplification is acceptable, as the fibre contribution is highly anisotropic. For the permeability it is probably a less accurate assumption and a transversely isotropic permeability would probably be more appropriate. However, the lack of experimental data in combination with the small influence that permeability has on the current model does not make it worth while to introduce additional material parameters describing permeability.

The reason permeability had so little impact on the current model is most likely due to the fact that the viscous behaviour is already captured by the collagen model. It is difficult to measure the permeability of tendons and therefore there is no experimental data to be found.

Maybe transverse mechanical testing could be used to better optimize the permeability values, as the viscous impact of the fibres are close to zero in that direction. The problem with anisotropy still remains, but it could result in more appropriate values for the permeability coefficient.

The optimization procedure in Matlab was slightly limited by the numerical instabilities in Abaqus. This meant that all initial parameters had to be set manually to fairly match the experimental data and that the optimization algorithm had problems deviating too much from these values as that lead to divergence in Abaqus and huge residuals. The resulting material parameters still provide a good fit even though it cannot be concluded that the solution is a global optimum.

One of the main assumptions made in this model is that the fibres are longitudinally aligned. This a reasonable assumption for fully pre-constrained tendons but if that is not the case then there are crimp formations in the tendon. This model does not model crimp in a structural way but the behaviour is described by the material parameters. To improve the model, the fibres could be modelled as wavy in the initial configuration to mimic the crimps, for example by giving the direction vectors $\mathbf{e}_0$ a random or zig-zag orientation. There are examples in literature where the structural fibre distribution is considered and the gradual straightening of the fibres (often called fibre recruitment) is modelled. The fibre distributions are often modelled with different kinds of probability functions, see for example (Sverdlik and Lanir, 2002; Einat and Lanir, 2009). Incorporating the fibre recruitment in this model would probably improve the ability to predict creep.

6   Conclusions

A new structural finite element model, including collagen fibres, ground substance and fluid flow, was developed for the Achilles tendon. The model was successfully fitted to experimental test data from two different data sets and no visual differences were found between the sets.

This project shows that it was possible to use a model developed for articular cartilage loaded in unconfined compression and adapt it for the Achilles tendon subjected to cyclic tensile loading. This structural model captures the mechanical behaviour of the components of the Achilles tendon and indicates that the collagen fibres are the most important load-bearing structures, which agrees with mechanical testing. In conclusion, this model can be used to simulate rat Achilles tendons subjected to cyclic loading and it looks promising for predicting the general mechanical behaviour of the Achilles tendon under different loading conditions.

7 Future work

The model presented in this master's thesis can be a starting point for a more comprehensive model for the Achilles tendon. An improved description of the collagen fibres is needed to capture the tendon's creep behaviour. This could be done by including the gradual straightening of the fibres when subjected to loading, so called fibre recruitment.

Also, the model needs to be validated against other types of experimental test data, for example from stress-relaxation tests. Stress-relaxation data would probably also give more information about the fluid flow and the permeability in the tendon. Further studies on the fluid flow is important as the cells, and thereby the mechanobiological regulation of the tendon, are affected by the flow.

Finally, the greater aim is to apply the model on human Achilles tendons. This structural model, applied on a realistic 3D geometry, would provide information about both structure and local stresses in the tendon that could be a valuable tool for predicting and preventing tendon rupture and designing appropriate treatments for injured tendons.

8 Bibliography

Anitas, R. and Lucaciu, D. 2013. Finite Element Analysis of the Achilles Tendon While Running. *Acta Medica Marisiensis*, 59(1):8–11.

Bergström, J.S. and Boyce, M.C. 2001. Constitutive modeling of the time-dependent and cyclic loading of elastomers and application to soft biological tissues. *Mechanics of Materials*, 33(9):523–530.

Davis, F.M. and De Vita, R. 2012. A nonlinear constitutive model for stress relaxation in ligaments and tendons. *Annals of biomedical engineering*, 40(12):2541–50.

Einat, R. and Lanir, Y. 2009. Recruitment viscoelasticity of the tendon. *Journal of biomechanical engineering*, 131(11):111008.

Eliasson, P., Fahlgren, A., Pasternak, B., and Aspenberg, P. 2007. Unloaded rat Achilles tendons continue to grow, but lose viscoelasticity. *Journal of applied physiology (Bethesda, Md. : 1985)*, 103(2):459–63.

Franchi, M., Trirè, A., Quaranta, M., Orsini, E., and Ottani, V. 2007. Collagen structure of tendon relates to function. *The Scientific World Journal*, 7:404–20.

Freutel, M., Schmidt, H., Dürselen, L., Ignatius, A., and Galbusera, F. 2014. Finite element modeling of soft tissues: Material models, tissue interaction and challenges. *Clinical Biomechanics*.

Gautieri, A., Vesentini, S., Redaelli, A., and Ballarini, R. 2013. Modeling and measuring visco-elastic properties: From collagen molecules to collagen fibrils. *International Journal of Non-Linear Mechanics*, 56:25–33.

Gupta, H.S., Seto, J., Krauss, S., Boesecke, P., and Screen, H.R.C. 2010. In situ multi-level analysis of viscoelastic deformation mechanisms in tendon collagen. *Journal of structural biology*, 169(2):183–91.

Heuijerjans, A. 2012. Modeling of the Achilles tendon. Technical report, Solid Mechanics, Lund University, Supervisor: Hanna Isaksson, Lund.

Holm, C, Kjaer, M, and Eliasson, P. 2014. Achilles tendon rupture - treatment and complications: A systematic review. *Scandinavian journal of medicine & science in sports*, pages 1–10.

Julkunen, P., Wilson, W., Jurvelin, J.S., Rieppo, J., Qu, C., Lammi, M.J., and Korhonen, R.K. 2008. Stressrelaxation of human patellar articular cartilage in unconfined compression: Prediction of mechanical response by tissue composition and structure. *Journal of Biomechanics*, 41(9):1978–1986.

Kahn, C.J.F., Dumas, D., Arab-Tehrany, E., Marie, V., Tran, N., Wang, X., and Cleymand, F. 2013. Structural and mechanical multi-scale characterization of white New-Zealand rabbit Achilles tendon. *Journal of the mechanical behavior of biomedical materials*, 26:81–9.

Ker, R. 2007. Mechanics of tendon, from an engineering perspective. *International Journal of Fatigue*, 29(6):1001–1009.

Korhonen, R.K. and Saarakkala, S. 2011. Biomechanics and Modeling of Skeletal Soft Tissues. In *Theoretical Biomechanics*, chapter Biomechani, pages 113–132. InTech.

Krenk, S. 2009. *Non-linear Modeling and Analysis of Solids and Structures*. Cambridge University Press, Cambridge, first edition.

Lanir, Y. 1978. Structure-strength relations in mammalian tendon. *Biophysical journal*, 24(2):541–54.

Lanir, Y. 1979. A structural theory for the homogeneous biaxial stress-strain relationships in flat collagenous tissues. *Journal of biomechanics*, 12(6):423–36.

Mak, A.F., Lai, W.M., and Mow, V.C. 1987. Biphasic indentation of articular cartilageI. Theoretical analysis. *Journal of Biomechanics*, 20(7):703–714.

Nordin, M. and Frankel, V.H. 2012. *Basic Biomechanics of the Musculoskeletal system*. Lippincott Williams and Wilkins, Philadelphia, fourth edition.

O'Brien, M. 2005. Anatomy of Tendons. In *Tendon Injuries*, chapter 1, pages 3–21. Springer-Verlag, London.

Provenzano, P. and Lakes, R. 2001. Nonlinear ligament viscoelasticity. *Annals of biomedical engineering*, 29:908–914.

Screen, H.R.C. 2008. Investigating load relaxation mechanics in tendon. *Journal of the mechanical behavior of biomedical materials*, 1(1):51–8.

Sverdlik, A. and Lanir, Y. 2002. Time-Dependent Mechanical Behavior of Sheep Digital Tendons, Including the Effects of Preconditioning. *Journal of Biomechanical Engineering*, 124(1):78.

Tang, C.Y., Ng, G.Y.F., Wang, Z.W., Tsui, C.P., and Zhang, G. 2011. Parameter optimization for the visco-hyperelastic constitutive model of tendon using FEM. *Bio-medical materials and engineering*, 21(1): 9–24.

van Loon, R., Huyghe, J.M., Wijlaars, M.W., and Baaijens, F.P.T. 2003. 3D FE implementation of an incompressible quadriphasic mixture model. *International Journal for Numerical Methods in Engineering*, 57(9):1243–1258.

Von Forell, G.A., Hyoung, P.S., and Bowden, A.E. 2014. Failure Modes and Fracture Toughness in Partially Torn Ligaments and Tendons. *Journal of the Mechanical Behavior of Biomedical Materials*.

Wang, J.H-C. 2006. Mechanobiology of tendon. *Journal of biomechanics*, 39(9):1563–82.

Wilson, W., van Donkelaar, C.C., van Rietbergen, B., Ito, K., and Huiskes, R. 2004. Stresses in the local collagen network of articular cartilage: a poroviscoelastic fibril-reinforced finite element study. *Journal of Biomechanics*, 37(3):357–366.

Wilson, W., van Donkelaar, C.C., and Huyghe, J.M. 2005a. A Comparison Between Mechano-Electrochemical and Biphasic Swelling Theories for Soft Hydrated Tissues. *Journal of Biomechanical Engineering*, 127(1):158.

Wilson, W., van Donkelaar, C.C., van Rietbergen, B., and Huiskes, R. 2005b. A fibril-reinforced poroviscoelastic swelling model for articular cartilage. *Journal of Biomechanics*, 38(6):1195–1204.

Wilson, W., Huyghe, J.M., and van Donkelaar, C.C. 2006. A composition-based cartilage model for the assessment of compositional changes during cartilage damage and adaptation. *Osteoarthritis and cartilage / OARS, Osteoarthritis Research Society*, 14(6):554–60.

Yamamoto, E., Hayashi, K., and Yamamoto, N. 2000. Effects of stress shielding on the transverse mechanical properties of rabbit patellar tendons. *Journal of biomechanical engineering*, 122(6):608–14.

Yin, L. and Elliott, D.M. 2004. A biphasic and transversely isotropic mechanical model for tendon: application to mouse tail fascicles in uniaxial tension. *Journal of biomechanics*, 37(6):907–16.

Appendix A - Sample geometries and meshes

In table 3 the lengths and radii are given for all samples. Sample 1209 - 1247 belong to the paralysed group in the study described in section 2.3 and sample 1265 - 1277 belong to the control group.

Table 3: List of all sample sizes and number of elements in each mesh

sample	length (mm)	radius (mm)	number of elements
1209	9.37	0.755	220
1210	7.58	0.744	180
1211	7.63	0.753	182
1215	9.14	0.615	216
1218	8.26	0.717	196
1219	8.58	0.645	200
1223	8.99	0.696	212
1224	10.02	0.671	236
1241	8.20	0.740	192
1242	9.55	0.664	224
1246	8.53	0.635	200
1247	9.07	0.702	212
mean	8.74	0.695	-
SD	0.75	0.05	-
1265	8.24	0.768	184
1267	8.98	0.641	240
1268	9.06	0.779	200
1269	8.14	0.721	192
1270	9.01	0.722	212
1272	8.17	0.781	180
1274	9.23	0.762	216
1275	8.34	0.752	196
1277	7.41	0.644	196
mean	8.51	0.73	-
SD	0.60	0.05	-

The mesh used for the average control tendon contains 200 elements and the average mesh for the paralysed group contains 204 elements.

Appendix B - Energy function for non-fibrillar solid matrix

The solid non-fibrillar matrix is modelled as a Neo-Hookean (hyperelastic) material defined by the following energy function

$$W_{nf} = \underbrace{\frac{K_m}{2}\left(\frac{1}{2}(J^2-1) - ln(J)\right)}_{W_1} + \underbrace{\frac{1}{2}G_m\left(tr(\mathbf{C}) - 3det(\mathbf{C})^{1/3}\right)}_{W_2} \quad (53)$$

The Cauchy stress $\boldsymbol{\sigma}$ is derived from the energy function as

$$\boldsymbol{\sigma}_{nf} = \frac{2}{J}\mathbf{F}\frac{\partial W_{nf}}{\partial \mathbf{C}}\mathbf{F}^T \quad (54)$$

where J is the Jacobian of the deformation tensor $\mathbf{F}$ and $\mathbf{C}$ is the right Cauchy-Green tensor defined as

$$\mathbf{C} = \mathbf{F}^T\mathbf{F} \quad (55)$$

The following derivatives are useful to calculate (54)

$$\frac{\partial J}{\partial \mathbf{F}} = J\mathbf{F}^{-T} \quad (56)$$

$$\frac{\partial J}{\partial \mathbf{C}} = \frac{J}{2}\mathbf{F}^{-1}\mathbf{F}^{-T} = \frac{J}{2}\mathbf{C}^{-1} \quad (57)$$

For simplicity, the derivation is carried out separately for W_1 and W_2, defined in (53). The derivative of the first part of (53) with respect to the right Cauchy-Green deformation tensor is

$$\frac{\partial W_1}{\partial \mathbf{C}} = \frac{\partial W_1}{\partial J}\frac{\partial J}{\partial \mathbf{C}} = \frac{\partial}{\partial J}\left(\frac{K_m}{2}\left[\frac{1}{2}(J^2-1) - ln(J)\right]\right)\frac{J}{2}\mathbf{C}^{-1} = \quad (58)$$

$$= \frac{K_m}{2}\left(\frac{1}{2}2J - \frac{1}{J}\right)\frac{J}{2}\mathbf{C}^{-1} = \frac{K_m}{4}\left(J^2-1\right)\mathbf{C}^{-1}$$

Inserting (58) into (54) gives

$$\boldsymbol{\sigma}_1 = \frac{2}{J}\mathbf{F}\frac{K_m}{4}\left(J^2-1\right)\mathbf{C}^{-1}\mathbf{F}^T \quad (59)$$

and with the definition in (55) it simplifies to

$$\boldsymbol{\sigma}_1 = \frac{K_m}{2}\left(J - \frac{1}{J}\right)\mathbf{F}\mathbf{F}^{-1}\mathbf{F}^{-T}\mathbf{F}^T = \frac{K_m}{2}\left(J - \frac{1}{J}\right)\mathbf{I} \quad (60)$$

where $\mathbf{I}$ is the unit tensor.

For the second part the following derivatives of the trace and determinant of the tensor A are useful

$$\frac{\partial tr(\mathbf{A})}{\partial \mathbf{A}} = \mathbf{I} \quad (61)$$

$$\frac{\partial det(\mathbf{A})}{\partial \mathbf{A}} = det(\mathbf{A})\mathbf{A}^{-T} \tag{62}$$

The derivative of the second part of (53) with respect to the right Cauchy-Green tensor is

$$\frac{\partial W_2}{\partial \mathbf{C}} = \frac{G_m}{2}\frac{\partial}{\partial \mathbf{C}}\left(tr(\mathbf{C}) - 3det(\mathbf{C})^{1/3}\right) =$$

$$\frac{G_m}{2}\left(\mathbf{I} - 3\frac{1}{3}det(\mathbf{C})^{-2/3}\frac{\partial det(\mathbf{C})}{\partial \mathbf{C}}\right) =$$

$$= \frac{G_m}{2}\left(\mathbf{I} - 3\frac{1}{3}det(\mathbf{C})^{-2/3}det(\mathbf{C})\mathbf{C}^{-T}\right) = \frac{G_m}{2}\mathbf{I} - det(\mathbf{C})^{1/3}\mathbf{C}^{-T} \tag{63}$$

With the following relationship in mind

$$det(\mathbf{C}) = det(\mathbf{F}^T\mathbf{F}) = J^2 \tag{64}$$

the derivative of the second part can be simplified to

$$\frac{\partial W_2}{\partial \mathbf{C}} = \frac{G_m}{2}\left(\mathbf{I} - (J^2)^{1/3}\mathbf{F}^{-1}\mathbf{F}^{-T}\right) = \frac{G_m}{2}\left(\mathbf{I} - J^{2/3}\mathbf{F}^{-1}\mathbf{F}^{-T}\right) \tag{65}$$

Inserting (65) into (54) gives

$$\boldsymbol{\sigma}_2 = \frac{2}{J}\mathbf{F}\frac{G_m}{2}\left(\mathbf{I} - J^{2/3}\mathbf{F}^{-1}\mathbf{F}^{-T}\right)\mathbf{F}^T = \frac{G_m}{J}\left(\mathbf{F}\mathbf{F}^T - J^{2/3}I\right) \tag{66}$$

Equation (66) can be expressed in terms of the left Cauchy-Green deformation tensor

$$\mathbf{B} = \mathbf{F}\mathbf{F}^T \tag{67}$$

so that

$$\boldsymbol{\sigma}_2 = \frac{G_m}{J}\left(\mathbf{B} - J^{2/3}\mathbf{I}\right) \tag{68}$$

The sum of (60) and (68)give the total non-fibrillar stress

$$\boldsymbol{\sigma}_{nf} = \frac{K_m}{2}\left(J - \frac{1}{J}\right)\mathbf{I} + \frac{G_m}{J}\left(\mathbf{B} - J^{2/3}\mathbf{I}\right) \tag{69}$$

Appendix C - Results from optimization

Control group
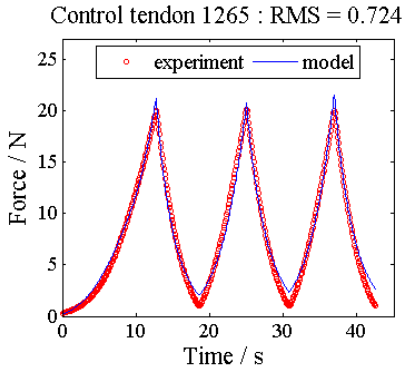
Figure 19: Specimen 1265
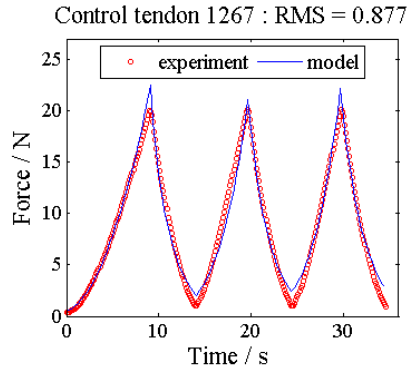
Figure 20: Specimen 1267
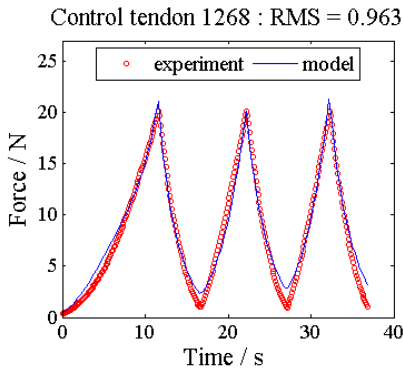
Figure 21: Specimen 1268
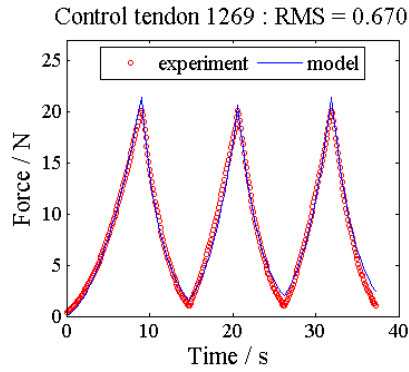
Figure 22: Specimen 1269
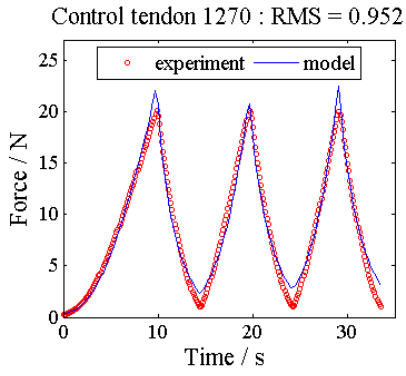
Figure 23: Specimen 1270
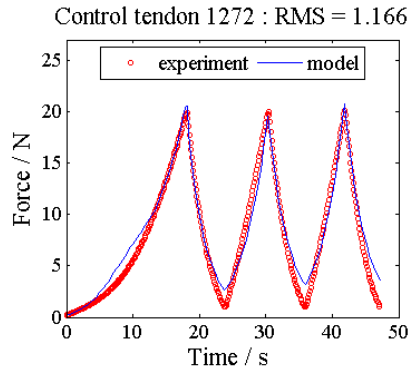
Figure 24: Specimen 1272
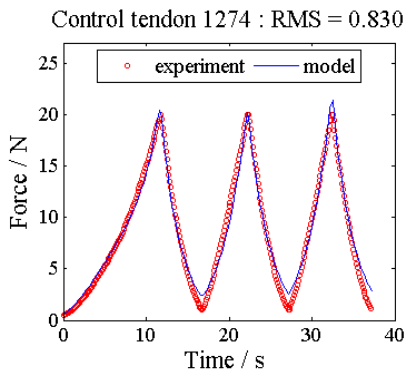
Figure 25: Specimen 1274
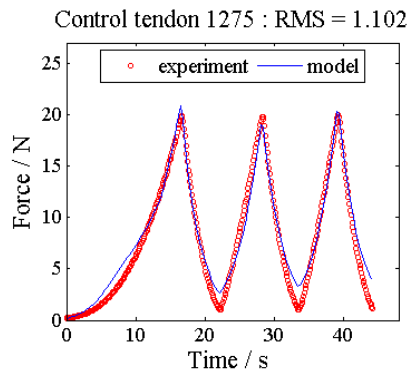
Figure 26: Specimen 1275
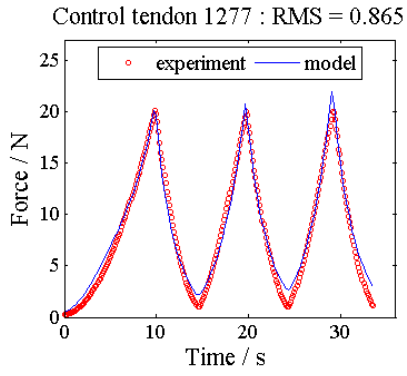
Figure 27: Specimen 1277

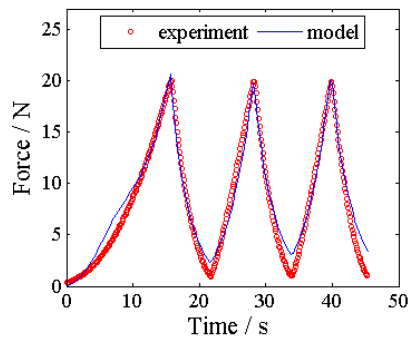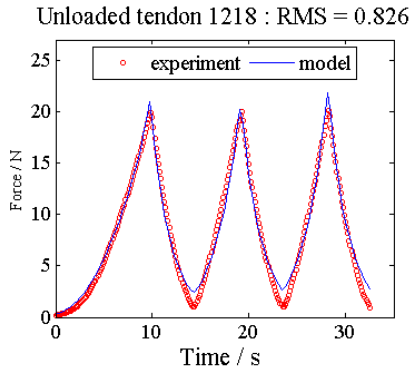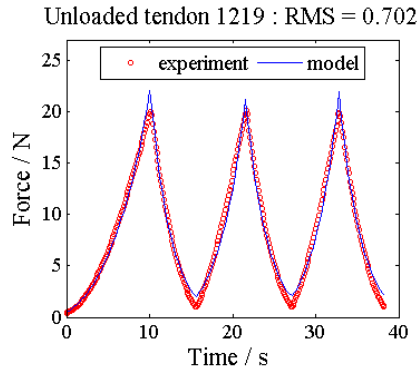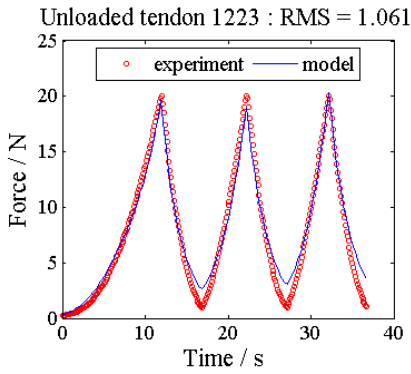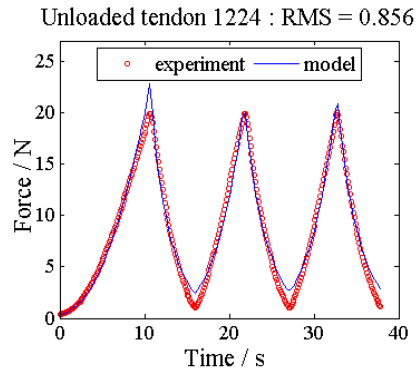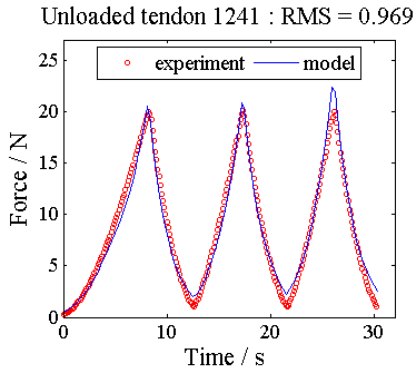## Paralysed group
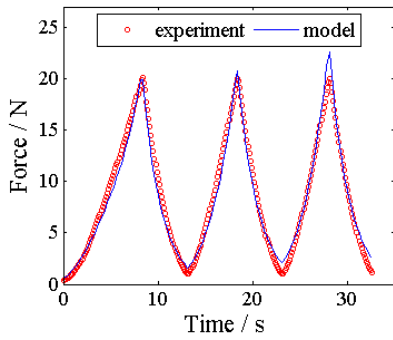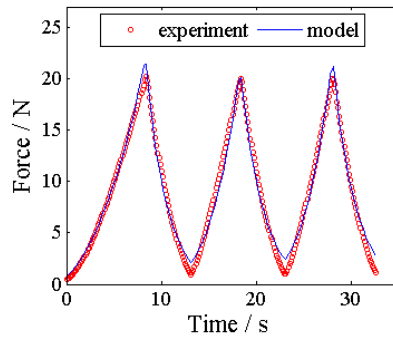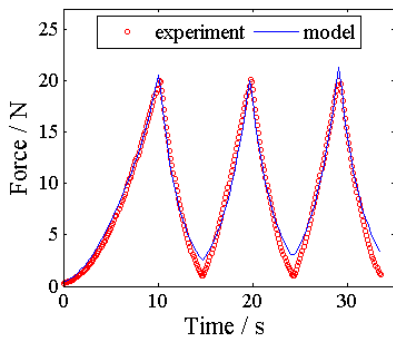
Figure 28: Specimen 1209

Figure 29: Specimen 1210

Figure 30: Specimen 1211

Figure 31: Specimen 1215
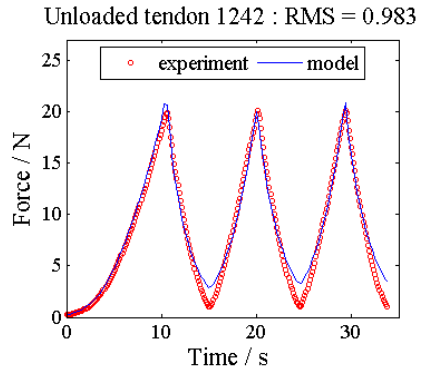
Figure 32: Specimen 1218

Figure 33: Specimen 1219

Figure 34: Specimen 1223

Figure 35: Specimen 1224
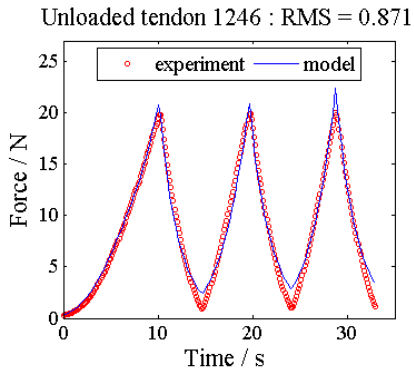
Figure 36: Specimen 1241
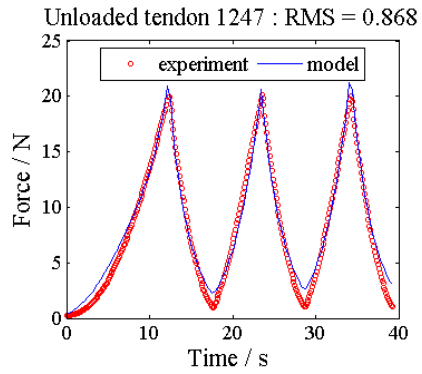

Figure 37: Specimen 1242

Figure 38: Specimen 1246

Figure 39: Specimen 1247